



**HAL**  
open science

## The end of the isotopic evolution of atmospheric xenon

L. Ardoin, M.W. Broadley, M. Almayrac, Guillaume Avice, D.J. Byrne, A. Tarantola, A. Lepland, T. Saito, T. Komiya, T. Shibuya, et al.

### ► To cite this version:

L. Ardoin, M.W. Broadley, M. Almayrac, Guillaume Avice, D.J. Byrne, et al.. The end of the isotopic evolution of atmospheric xenon. *Geochemical Perspectives Letters*, 2022, 20, pp.43-47. 10.7185/geochemlet.2207 . hal-03693285

**HAL Id: hal-03693285**

**<https://hal.science/hal-03693285>**

Submitted on 4 Oct 2022

**HAL** is a multi-disciplinary open access archive for the deposit and dissemination of scientific research documents, whether they are published or not. The documents may come from teaching and research institutions in France or abroad, or from public or private research centers.

L'archive ouverte pluridisciplinaire **HAL**, est destinée au dépôt et à la diffusion de documents scientifiques de niveau recherche, publiés ou non, émanant des établissements d'enseignement et de recherche français ou étrangers, des laboratoires publics ou privés.

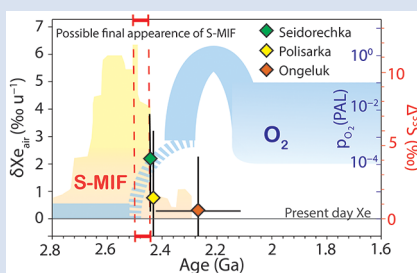
## The end of the isotopic evolution of atmospheric xenon

L. Ardoin<sup>1,2\*</sup>, M.W. Broadley<sup>1</sup>, M. Almayrac<sup>1</sup>, G. Avice<sup>3</sup>, D.J. Byrne<sup>1</sup>, A. Tarantola<sup>4</sup>,  
A. Lepland<sup>5</sup>, T. Saito<sup>6</sup>, T. Komiya<sup>7</sup>, T. Shibuya<sup>6</sup>, B. Marty<sup>1</sup>



<https://doi.org/10.7185/geochemlet.2207>

### Abstract



Noble gases are chemically inert and, as such, act as unique tracers of physical processes over geological timescales. The isotopic composition of atmospheric xenon, the heaviest stable noble gas, evolved following mass-dependent fractionation throughout the Hadean and Archaean aeons. This evolution appears to have ceased between 2.5 and 2.1 Ga, around the time of the Great Oxidation Event (GOE). The coincidental halting of atmospheric Xe evolution may provide further insights into the mechanisms affecting the atmosphere at the Archaean-Proterozoic transition. Here, we investigate the isotopic composition of Xe trapped in hydrothermal quartz from three formations around the GOE time period: Seidorechka and Polisarka (Imandra-Varzuga Greenstone Belt, Kola Craton, Russia) with ages of  $2441 \pm 1.6$  Ma and  $2434 \pm 6.6$  Ma, respectively, and Ongeluk (Kaapvaal Craton, South Africa) dated at  $2114 \pm 312$  Ma (Ar-Ar age) with a host formation age of  $2425.6 \pm 2.6$  Ma (upper bound). From these analyses we show that Xe isotope fractionation appears to have ceased during the time window delimited by the ages of the Seidorechka and Polisarka Formations, which is concomitant with the disappearance of mass-independent fractionation of sulfur isotopes (MIF-S) in the Kola Craton. The disappearance of Xe isotope fractionation in the geological record may be related to the rise in atmospheric oxygen and, thus, can provide new insights into the triggering mechanisms and timing of the GOE.

Received 29 October 2021 | Accepted 1 February 2022 | Published 10 March 2022

### Introduction

Due to their chemical inertness, noble gases (He, Ne, Ar, Kr, Xe) constitute powerful geochemical tracers for constraining physical processes occurring in the Earth's atmosphere. Atmospheric xenon is of particular interest because its isotopic composition is highly mass-dependently fractionated (MDF) by  $41.5 \text{‰ u}^{-1}$  when compared to its presumed primitive ancestor U-Xe (Pepin, 1991). Studies of palaeo-atmospheric Xe trapped in Archaean rocks (mainly as fluid inclusions in hydrothermal quartz) have shown that the evolution of isotopic fractionation of Xe was a long-term process that took place during the Hadean and the Archaean aeons. This protracted MDF appears to be unique to Xe, with no evidence that the other noble gases underwent progressive fractionation (Pujol *et al.*, 2011; Avice *et al.*, 2018; Almayrac *et al.*, 2021). Such Xe specific evolution has been attributed to preferential, non-thermal escape of xenon from the Earth's atmosphere to space upon ionisation by solar UV photons (Pujol *et al.*, 2011; Hébrard and Marty, 2014; Avice *et al.*, 2018) and subsequent entrainment by escaping hydrogen ions (Zahnle *et al.*, 2019). Available data indicate

that the evolution of the isotopic composition of atmospheric xenon ceased at some point between 2.6 and 1.8 Ga (Avice *et al.*, 2018).

Xenon is the second atmospheric element for which a stable isotope fractionation during the Archaean aeon has been observed, with the mass-independent fractionation of sulfur isotopes (MIF-S) being characteristic for Archaean age samples (Farquhar and Wing, 2003; Philippot *et al.*, 2018). The MIF-S signature was likely produced by interactions between volcanic sulfur species and ultraviolet radiation, and shows a sharp transition and collapse during the Great Oxidation Event (GOE) (Farquhar and Wing, 2003). Conversely, the Xe isotope evolution was a gradual and cumulative process, causing atmospheric Xe to become increasingly fractionated with time. Furthermore, the GOE is understood to have stopped the generation of MIF-S, as ozone from free oxygen in the atmosphere shielded solar UV photons. For Xe, it is not clear if the GOE was also responsible for stopping Xe<sup>+</sup> escape, and which environmental parameters (*e.g.*, atmospheric composition, hydrogen escape, solar activity) may have changed to prevent Xe from escaping the Earth's atmosphere.

1. Université de Lorraine, CNRS, CRPG, F-54000 Nancy, France
2. Now at: Université Libre de Bruxelles CP160/03 Av. F.D. Roosevelt 50, 1050 Brussels, Belgium
3. Université de Paris, Institut de physique du globe de Paris, CNRS, F-75005 Paris, France
4. Université de Lorraine, CNRS, GeoRessources laboratory, BP 70239, F-54506, Vandœuvre-lès-Nancy, France
5. Geological Survey of Norway, 7491 Trondheim, Norway
6. Institute for Extra-cutting-edge Science and Technology Avant-garde Research (X-star), Japan Agency for Marine-Earth Science and Technology (JAMSTEC), 2-15, Natsushima-cho, Yokosuka 237-0061, Japan
7. Department of Earth Science and Astronomy, University of Tokyo, Tokyo, Meguro, 153-8902, Japan

\* Corresponding author (email: [lisa.ardoin@ulb.be](mailto:lisa.ardoin@ulb.be))



In order to investigate the end of atmospheric MDF-Xe and to assess if it was coincidental with the GOE, we have analysed noble gases extracted from fluid inclusions from well-characterised hydrothermal quartz with ages encompassing that of the GOE. Using a new cumulative crushing technique, adapted from the procedure first used by Péron and Moreira (2018), allows the extraction of gas from much larger sample quantities, resulting in smaller analytical uncertainties (Supplementary Information). This is required to detect the low levels of Xe fractionation relative to the modern atmosphere that are observed close to the GOE. The samples measured in this study are, from oldest to youngest, Seidorechka (FD1A) and Polisarka (FD3A) Sedimentary Formations (Imandra-Varzuga Greenstone Belt, Kola Craton, Russia), and from the Ongeluk Formation (Kaapvaal Craton, South Africa). Depositional ages of FD1A and FD3A have been constrained between  $2501.5 \pm 1.7$  Ma and  $2441 \pm 1.6$  Ma (Amelin *et al.*, 1995), and  $2441 \pm 1.6$  Ma and  $2434 \pm 6.6$  Ma (Brasier *et al.*, 2013), respectively. The lower bounds of these time intervals are defined by the ages of overlying volcanic formations that are considered contemporaneous with quartz veining in underlying sediments.

The Ongeluk Formation has been dated at  $2114 \pm 312$  Ma (Ar-Ar age; Saito *et al.*, 2018) with an upper bound defined by the host formation age of  $2425.6 \pm 2.6$  Ma (Gumsley *et al.*, 2017).

## Preservation of Ancient Atmospheric Xe

Fluid inclusions can potentially preserve the noble gas signature of the ancient atmosphere (Pujol *et al.*, 2011). The petrographical study of the inclusions of the Ongeluk Formation performed by Saito *et al.* (2018) and our study of samples from the Kola Craton (FD1A and FD3A) indicate that a majority of the fluid inclusions have been trapped during quartz growth (Supplementary Information). The Ar and Xe content of the quartz fluid inclusions were measured using a ThermoFisher Helix MC Plus® mass spectrometer at CRPG. The new extraction method was performed on FD1A and FD3A and consists of accumulating the extracted gases after crushing steps in an empty and previously evacuated steel bottle (Péron and Moreira, 2018; Péron *et al.*, 2021).

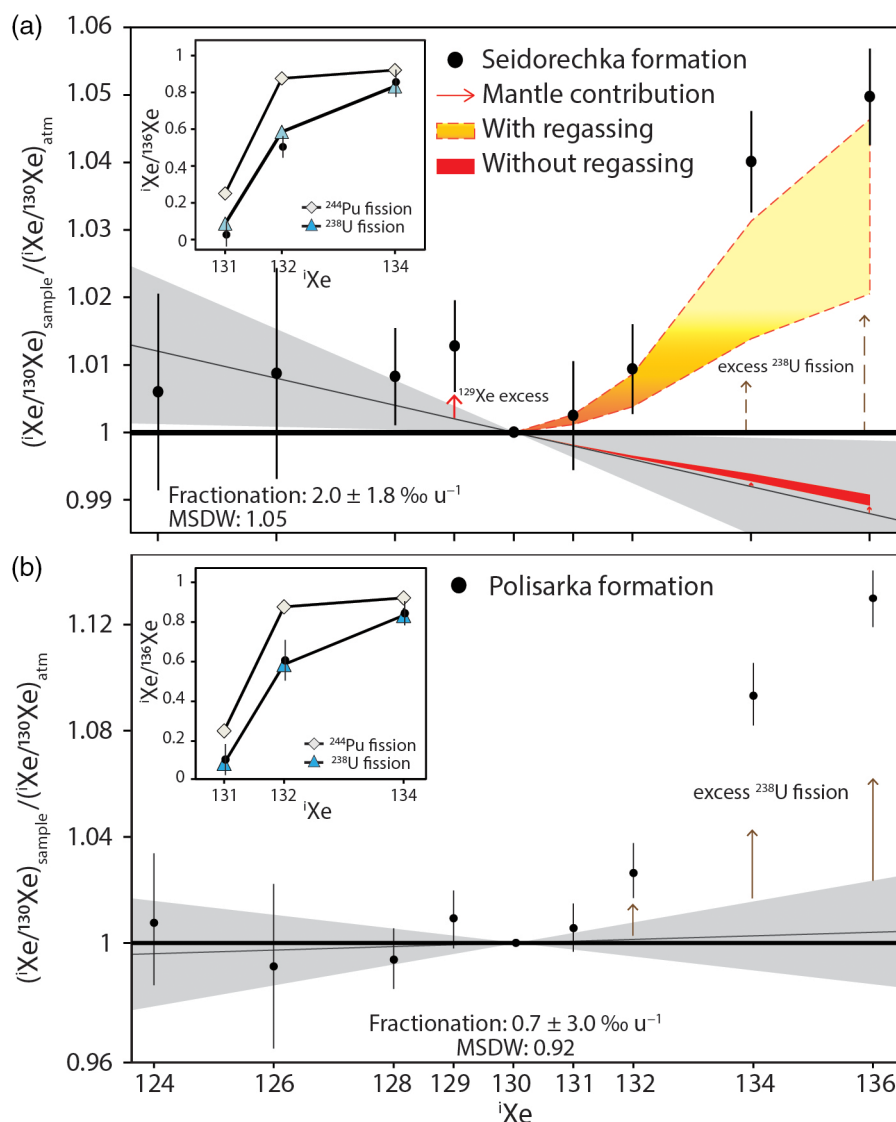


**Figure 1** Isotopic spectrum of Xe released from fluid inclusions in (a) sample FD1A and (b) sample FD3A. The grey line and its associated envelope ( $2\sigma$ ) correspond to the isotopic trend of the  $^{124,126,128,130}\text{Xe}$ . (a) Mantle excesses of  $^{131,132,134,136}\text{Xe}$  are estimated using the  $^{129}\text{Xe}$  excess (Supplementary Information). Individual error bars are at  $2\sigma$ .

**Table 1** Isotopic ratio of the noble gases released by crushing and Xe fractionation. The fractionation was calculated from the  $^{124,126,128}\text{Xe}/^{130}\text{Xe}$  ratios. The ratios are the weighted average of several replicates (Table S-3).

| Samples                         | $^{124}\text{Xe}$     | $^{126}\text{Xe}$ | $^{128}\text{Xe}$ | $^{129}\text{Xe}$ | $^{131}\text{Xe}$ | $^{132}\text{Xe}$ | $^{134}\text{Xe}$ | $^{136}\text{Xe}$ | $^{40}\text{Ar}/^{36}\text{Ar}$ | Xe Fractionation (% $\text{u}^{-1}$ ) |
|---------------------------------|-----------------------|-------------------|-------------------|-------------------|-------------------|-------------------|-------------------|-------------------|---------------------------------|---------------------------------------|
|                                 | $^{130}\text{Xe} = 1$ |                   |                   |                   |                   |                   |                   |                   |                                 |                                       |
| Air<br>Ozima and Podosek (2002) | 0.0234                | 0.0218            | 0.4715            | 6.496             | 5.213             | 6.607             | 2.563             | 2.176             | 298                             |                                       |
| Ongeluk fm                      | 0.0233                | 0.0220            | 0.4707            | 6.540             | 5.188             | 6.632             | 2.603             | 2.229             | 4570                            | -0.3                                  |
| errors ( $2\sigma$ )            | $\pm 0.0005$          | $\pm 0.0004$      | $\pm 0.0040$      | $\pm 0.066$       | $\pm 0.050$       | $\pm 0.640$       | $\pm 0.220$       | $\pm 0.020$       | $\pm 1488$                      | $\pm 2.4$                             |
| FD1A                            | 0.0235                | 0.0220            | 0.4745            | 6.578             | 5.235             | 6.669             | 2.666             | 2.284             | 3010                            | -2.0                                  |
| errors ( $2\sigma$ )            | $\pm 0.0004$          | $\pm 0.0004$      | $\pm 0.0034$      | $\pm 0.026$       | $\pm 0.068$       | $\pm 0.044$       | $\pm 0.0192$      | $\pm 0.016$       | $\pm 504$                       | $\pm 1.8$                             |
| FD3A                            | 0.0235                | 0.0216            | 0.4684            | 6.554             | 5.243             | 6.778             | 2.801             | 2.458             | 3639                            | 0.7                                   |
| errors ( $2\sigma$ )            | $\pm 0.0006$          | $\pm 0.0006$      | $\pm 0.0054$      | $\pm 0.056$       | $\pm 0.044$       | $\pm 0.056$       | $\pm 0.028$       | $\pm 0.024$       | $\pm 610$                       | $\pm 3.0$                             |

All our analyses present an excess of  $^{40}\text{Ar}$  relative to modern atmospheric Ar with a minimum  $^{40}\text{Ar}/^{36}\text{Ar}$  ratio of  $1760 \pm 18$ , from one crush of the Ongeluk Formation (Table S-4), attesting to limited exchange, if any, with modern atmospheric Ar. The  $^{131,132,134,136}\text{Xe}$  excesses detected for all our samples correspond to a contribution from the spontaneous fission of  $^{238}\text{U}$  (Fig. 1). We computed linear regressions on  $^{124,126,128}\text{Xe}/^{130}\text{Xe}$  isotope ratios using the IsoplotR software (Vermeesch, 2018). The oldest sample, FD1A, presents a fractionation of  $2.0 \pm 1.8$  ‰  $\text{u}^{-1}$  ( $2\sigma$ ; Fig. 1a) compared to the present day atmosphere. The FD3A ( $0.7 \pm 3.3$  ‰  $\text{u}^{-1}$ , Fig. 1b) and Ongeluk quartz ( $-0.3 \pm 2.4$  ‰  $\text{u}^{-1}$ , Fig. S-2), the youngest samples, do not display a resolvable MDF-Xe signature beyond uncertainty at  $2\sigma$  (Table 1). Compared to modern atmospheric Xe ( $^{129}\text{Xe}/^{130}\text{Xe} = 6.50$ ; Ozima and Podosek, 2002), the samples preserve small excesses of radiogenic  $^{129}\text{Xe}$  ( $^{129}\text{Xe}/^{130}\text{Xe}$  of  $6.58 \pm 0.04$ ,  $6.55 \pm 0.06$  and  $6.54 \pm 0.07$  for FD1A, FD3A and Ongeluk Formation samples, respectively). It is the opposite of what is usually observed in samples from the Archaean aeon (Avice et al., 2017; Bekaert et al., 2018). The mono-isotopic depletion in  $^{129}\text{Xe}$  within the Archaean atmosphere is thought to have been compensated by the progressive release of  $^{129}\text{Xe}$  from the mantle throughout the Archaean aeon (Marty et al., 2019). The  $^{129}\text{Xe}$  excess in the oldest sample, FD1A, is therefore likely to be due to a local input of mantle-derived Xe in the hydrothermal fluids from which the quartz precipitated. A mantle Xe input could potentially account for the light Xe isotope excesses measured in the samples, especially when considering Xe in the Archaean mantle was likely primordial (chondritic; Broadley et al., 2020). We ruled out this possibility because the  $^{128}\text{Xe}/^{130}\text{Xe}$  of FD1A is inconsistent with mixing between the primordial mantle and modern atmosphere (Fig. S-4), and atmospheric regassing of the mantle was likely to be inefficient during the Archaean aeon (Péron and Moreira, 2018). Mantle contributions are then negligible (Table S-1; Supplementary Information) and excesses of  $^{124,126,128}\text{Xe}$  in FD1A are considered to reflect the ancient atmospheric composition.

## Link between Xe Fractionation and MIF-S

From our analyses we have shown, for the first time, that MDF-Xe signals disappear between two well-characterised Kola Craton sedimentary formations, implying that the fractionation process stopped between  $2441 \pm 1.6$  Ma and  $2434 \pm 6.6$  Ma (Fig. 2). Previous data from Avice et al. (2018) indicated that MDF-Xe was observable throughout the Archaean and into the Palaeoproterozoic era until 2 Ga. The difference between

these previous data and our new results can be explained by (i) the age of the fluid inclusions containing the atmospheric Xe, and (ii) the precision required to distinguish between the present day atmosphere and the small extent of isotope fractionation of Xe present in fluid inclusion formed close to the cessation of Xe evolution. The fluid inclusion inventory reflects the atmospheric composition at the last equilibration with the atmosphere, which may be different from the age of quartz precipitation. Thus, the  $6.5 \pm 1.5$  ‰  $\text{u}^{-1}$  recorded in the 3.7 Ga Isua rocks that was attributed to a resetting metamorphic event at 2.3 Ga (Avice et al., 2018) may, in fact, reflect an older atmospheric composition. Because the gas accumulation method is more precise than those used previously (Avice et al., 2018), we could identify a slight MDF-Xe for sample FD1A at the  $2\sigma$  precision level. Considering the  $2\sigma$  error range for the fractionation of Xe in previously studied  $2.1 \pm 0.1$  Ga Gaoua (Burkina Faso) and the  $2.0 \pm 0.1$  Ga Carnaiba (Brazil) samples gives values of  $2.6 \pm 4.2$  and  $1.8 \pm 4.4$  ‰  $\text{u}^{-1}$  for the fractionation of atmospheric Xe (Avice et al., 2018). These values are both within uncertainty of modern atmosphere, and therefore it is not clear whether they, in fact, contained a fractionated atmospheric Xe signature.

The MDF-Xe evolution results from a poorly understood cumulative process, which took place during the Hadean and Archaean periods. Storage of  $\text{Xe}^+$  into an organic haze and the contemporary loss of the residual Xe from space could explain the observed fractionation (Hébrard and Marty, 2014). This process would stop in an  $\text{O}_2$ -rich atmosphere that would halt the production of the haze. However, this possibility would still necessitate the escape of non-trapped Xe and therefore an additional, not yet identified, process is required. The escape of hydrogen ions to space entraining  $\text{Xe}^+$  has been also previously suggested to account for both the oxidation of the atmosphere and the unique fractionation of Xe isotopes (Zahnle et al., 2019). Consequently, this model leads to the oxidation of the surface reservoirs, including the crust, to the point where  $\text{O}_2$  became stable enough to compete with atmospheric reduced gases, such as  $\text{H}_2$  and  $\text{CH}_4$  (Zahnle et al., 2019). According to our data, the MDF-Xe signal disappears and the present day composition is reached between  $\sim 2441$  and  $\sim 2434$  Ma (Fig. 2). Sustaining a continuous escape of ionised hydrogen from the Earth formation until the GOE depends on many parameters including the strength of the Earth's magnetic field, the level of solar extreme ultraviolet (EUV) irradiation and the amount of hydrogen present in the atmosphere (Zahnle et al., 2019). In the case of discrete escape episodes rather than a constant rate of atmospheric Xe-loss, our results imply a final burst occurring simultaneously with the initiation of the GOE.

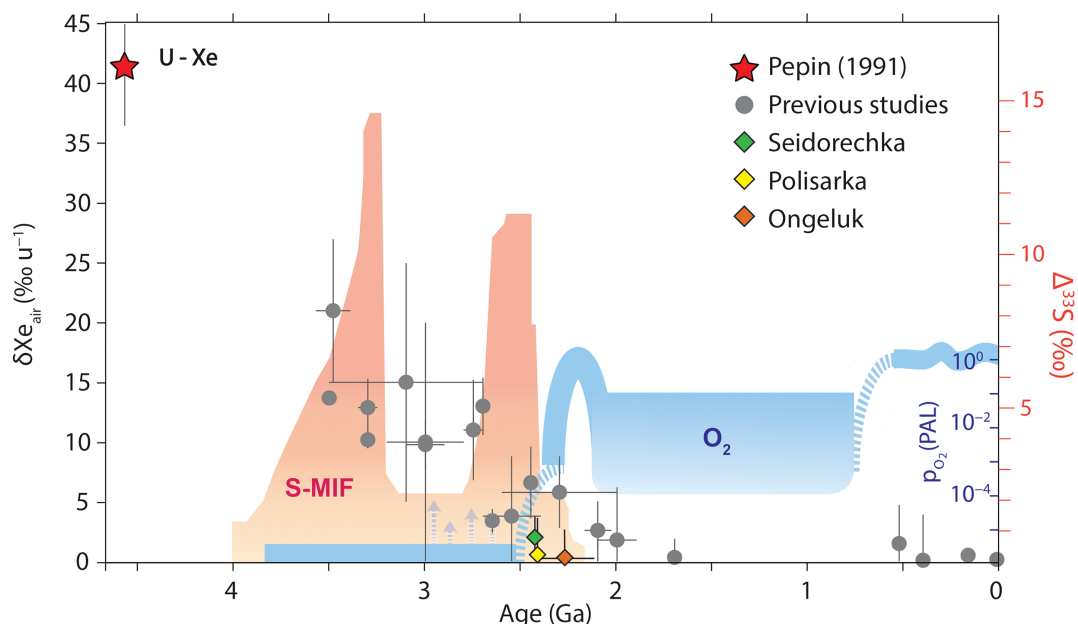


**Figure 2** Records of atmospheric oxygen ( $O_2$ , blue; Lyons *et al.*, 2014), mass-independent fractionation of sulfur isotopes (MIF-S, orange; data from Killingsworth *et al.*, 2019) and mass dependent fractionation of xenon isotopes throughout Earth's history (Pepin, 1991; Avice *et al.*, 2018; Almayrac *et al.*, 2021), uncertainties are at  $2\sigma$ .

The end of MDF-Xe between FD1A and FD3A is coincident with the disappearance of MIF-S as recorded in the sedimentary rocks hosting the quartz veins (Warke *et al.*, 2020). Sulfur isotopes represent an instantaneous record of the oxidation states of the atmosphere, at a local scale. MDF-Xe is the result of a cumulative process at global scale so it is likely that these geochemical markers would not be exactly simultaneous in their cessation. In light of the S-Xe relationship, it appears that the atmospheric process traced by Xe isotopes is linked with the oxidation state of the terrestrial atmosphere (Avice *et al.*, 2018).

The formation of the ozone layer as a consequence of  $O_2$  rise in the atmosphere accounts for the end of the MIF-S signature (Farquhar and Wing, 2003; Lyons *et al.*, 2014). However, MIF-S signals could be preserved under oxidative weathering and then obscure the MIF/MDF transition due to a memory effect (Philippot *et al.*, 2018). This leads to a delay between the rise of oxygen and the disappearance of MIF-S signals of about 2.32 Ga (Gumsley *et al.*, 2017; Poulton *et al.*, 2021). Moreover, some environments may require more time to adapt and become permanently oxygenated after the end of hydrogen escape (Lyons *et al.*, 2014). Contrary to the MIF-S, hydrodynamic escape is not affected by the ozone formation (Zahnle *et al.*, 2019), and may be more sensitive to  $O_2$  availability. Thus, the end of MDF-Xe fractionation could mark the time when atmospheric escape of hydrogen ceased, and ceased to contribute to the change of the redox ratio of Earth's surface reservoirs. It is important to underline the fact that Xe fractionation is a cumulative process: local variation of the signal cannot occur, unlike sulfur (Philippot *et al.*, 2018). In light of this, Xe is a reliable tracer and may better constrain the rise of oxygen levels within the atmosphere.

## Conclusion

We have measured an isotopically fractionated Xe composition of  $2.0 \pm 1.8 \text{ ‰ u}^{-1}$  relative to modern atmosphere at  $2441 \pm 1.6 \text{ Ma}$ . A slightly younger sample of  $2434 \pm 6.6 \text{ Ma}$  does not record any such fractionation, and is indistinguishable from the modern atmospheric composition. The disappearance of

isotopically fractionated Xe signals could be a consequence of  $O_2$  accumulation in the atmosphere. A temporal link between the disappearance of the Xe isotopes fractionation and the MIF-S signature at the Archaean-Proterozoic transition is clearly established for the Kola Craton. The mass-dependent evolution of Xe isotopes is the indication of a cumulative atmospheric process that may have played an important role in the oxidation of the Earth's surface (Zahnle *et al.*, 2019), independently of biogenic  $O_2$  production that started long before the permanent rise of  $O_2$  in the atmosphere (Lyons *et al.*, 2014).

## Acknowledgements

This study was supported by the European Research Council (ERC) under the European Union's Horizon 2020 research and innovation programme (PHOTONIS Advanced Grant # 695618). We thank the Super-Cutting-Edge Grand and Advanced Research (SUGAR) Program, Institute for Extra-Cutting-Edge Science and Technology Avant-Garde Research (X-star). We thank Laurent Zimmerman for technical mentorship and assistance. Christophe Thomazo is thanked for the sampling opportunity. The anonymous reviewers are thanked for their constructive suggestions.

Editor: Maud Boyet

## Additional Information

Supplementary Information accompanies this letter at <https://www.geochemicalperspectivesletters.org/article2207>.



© 2022 The Authors. This work is distributed under the Creative Commons Attribution Non-Commercial No-Derivatives 4.0

License, which permits unrestricted distribution provided the original author and source are credited. The material may not be adapted (remixed, transformed or built upon) or used for

commercial purposes without written permission from the author. Additional information is available at <https://www.geochemicalperspectivesletters.org/copyright-and-permissions>.

**Cite this letter as:** Ardoin, L., Broadley, M.W., Almayrac, M., Avice, G., Byrne, D.J., Tarantola, A., Lepland, A., Saito, T., Komiya, T., Shibuya, T., Marty, B. (2022) The end of the isotopic evolution of atmospheric xenon. *Geochem. Persp. Let.* 20, 43–47. <https://doi.org/10.7185/geochemlet.2207>

## References

- ALMAYRAC, M.G., BROADLEY, M.W., BEKAERT, D.V., HOFMANN, A., MARTY, B. (2021) Possible discontinuous evolution of atmospheric xenon suggested by Archean barites. *Chemical Geology* 581, 120405. <https://doi.org/10.1016/j.chemgeo.2021.120405>
- AMELIN, YU. V., HEAMAN, L.M., SEMENOV, V.S. (1995) U–Pb geochronology of layered mafic intrusions in the eastern Baltic Shield: Implications for the timing and duration of Paleoproterozoic continental rifting. *Precambrian Research* 75, 31–46. [https://doi.org/10.1016/0301-9268\(95\)00015-W](https://doi.org/10.1016/0301-9268(95)00015-W)
- AVICE, G., MARTY, B., BURGESS, R. (2017) The origin and degassing history of the Earth's atmosphere revealed by Archean xenon. *Nature Communications* 8, 15455. <https://doi.org/10.1038/ncomms15455>
- AVICE, G., MARTY, B., BURGESS, R., HOFMANN, A., PHILIPPOT, P., ZAHNLE, K., ZAKHAROV, D. (2018) Evolution of atmospheric xenon and other noble gases inferred from Archean to Paleoproterozoic rocks. *Geochimica et Cosmochimica Acta* 232, 82–100. <https://doi.org/10.1016/j.gca.2018.04.018>
- BEKAERT, D.V., BROADLEY, M.W., DELARUE, F., AVICE, G., ROBERT, F., MARTY, B. (2018) Archean kerogen as a new tracer of atmospheric evolution: Implications for dating the widespread nature of early life. *Science Advances* 4, eaar2091. <https://doi.org/10.1126/sciadv.aar2091>
- BRASIER, A.T., MARTIN, A.P., MELEZHIK, V.A., PRAVE, A.R., CONDON, D.J., FALICK, A.E. (2013) Earth's earliest global glaciation? Carbonate geochemistry and geochronology of the Polisarka Sedimentary Formation, Kola Peninsula, Russia. *Precambrian Research* 235, 278–294. <https://doi.org/10.1016/j.precamres.2013.06.007>
- BROADLEY, M.W., BARRY, P.H., BEKAERT, D.V., BYRNE, D.J., CARACAUSI, A., BALLENTINE, C.J., MARTY, B. (2020) Identification of chondritic krypton and xenon in Yellowstone gases and the timing of terrestrial volatile accretion. *Proceedings of the National Academy of Sciences* 117, 13997–14004. <https://doi.org/10.1073/pnas.2003907117>
- FARQUHAR, J., WING, B.A. (2003) Multiple sulfur isotopes and the evolution of the atmosphere. *Earth and Planetary Science Letters* 213, 1–13. [https://doi.org/10.1016/S0012-821X\(03\)00296-6](https://doi.org/10.1016/S0012-821X(03)00296-6)
- GUMSLEY, A.P., CHAMBERLAIN, K.R., BLEEKER, W., SÖDERLUND, U., DE KOCK, M.O., LARSSON, E.R., BEKKER, A. (2017) Timing and tempo of the Great Oxidation Event. *Proceedings of the National Academy of Sciences* 114, 1811–1816. <https://doi.org/10.1073/pnas.1608824114>
- HÉBRARD, E., MARTY, B. (2014) Coupled noble gas–hydrocarbon evolution of the early Earth atmosphere upon solar UV irradiation. *Earth and Planetary Science Letters* 385, 40–48. <https://doi.org/10.1016/j.epsl.2013.10.022>
- KILLINGSWORTH, B.A., SANSJOFRE, P., PHILIPPOT, P., CARTIGNY, P., THOMAZO, C., LALONDE, S.V. (2019) Constraining the rise of oxygen with oxygen isotopes. *Nature Communications* 10, 4924. <https://doi.org/10.1038/s41467-019-12883-2>
- LYONS, T.W., REINHARD, C.T., PLANAVSKY, N.J. (2014) The rise of oxygen in Earth's early ocean and atmosphere. *Nature* 506, 307–315. <https://doi.org/10.1038/nature13068>
- MARTY, B., BEKAERT, D.V., BROADLEY, M.W., JAUPART, C. (2019) Geochemical evidence for high volatile fluxes from the mantle at the end of the Archaean. *Nature* 575, 485–488. <https://doi.org/10.1038/s41586-019-1745-7>
- OZIMA, M., PODOSEK, F.A. (2002) *Noble Gas Geochemistry*. Second Edition, Cambridge University Press, Cambridge. <https://doi.org/10.1017/CBO9780511545986>
- PEPIN, R.O. (1991) On the origin and early evolution of terrestrial planet atmospheres and meteoritic volatiles. *Icarus* 92, 2–79. [https://doi.org/10.1016/0019-1035\(91\)90036-S](https://doi.org/10.1016/0019-1035(91)90036-S)
- PÉRON, S., MOREIRA, M. (2018) Onset of volatile recycling into the mantle determined by xenon anomalies. *Geochemical Perspectives Letters* 9, 21–25. <https://doi.org/10.7185/geochemlet.1833>
- PÉRON, S., MUKHOPADHYAY, S., KURZ, M.D., GRAHAM, D.W. (2021) Deep-mantle krypton reveals Earth's early accretion of carbonaceous matter. *Nature* 600, 462–467. <https://doi.org/10.1038/s41586-021-04092-z>
- PHILIPPOT, P., ÁVILA, J.N., KILLINGSWORTH, B.A., TESSALINA, S., BATON, F., CAQUINEAU, T., MULLER, E., PECOITS, E., CARTIGNY, P., LALONDE, S.V., IRELAND, T.R., THOMAZO, C., VAN KRANENDONK, M.J., BUSIGNY, V. (2018) Globally asynchronous sulphur isotope signals require re-definition of the Great Oxidation Event. *Nature Communications* 9, 2245. <https://doi.org/10.1038/s41467-018-04621-x>
- POULTON, S.W., BEKKER, A., CUMMING, V.M., ZERKLE, A.L., CANFIELD, D.E., JOHNSTON, D.T. (2021) A 200-million-year delay in permanent atmospheric oxygenation. *Nature* 592, 232–236. <https://doi.org/10.1038/s41586-021-03393-7>
- PUJOL, M., MARTY, B., BURGESS, R. (2011) Chondritic-like xenon trapped in Archean rocks: A possible signature of the ancient atmosphere. *Earth and Planetary Science Letters* 308, 298–306. <https://doi.org/10.1016/j.epsl.2011.05.053>
- SAITO, T., QIU, H.N., SHIBUYA, T., LI, Y.B., KITAJIMA, K., YAMAMOTO, S., UEDA, H., KOMIYA, T., MARUYAMA, S. (2018) Ar–Ar dating for hydrothermal quartz from the 2.4 Ga Ongeluk Formation, South Africa: Implications for seafloor hydrothermal circulation. *Royal Society Open Science* 5, 180260. <https://doi.org/10.1098/rsos.180260>
- VERMEESCH, P. (2018) IsoplotR: A free and open toolbox for geochronology. *Geoscience Frontiers* 9, 1479–1493. <https://doi.org/10.1016/j.gsf.2018.04.001>
- WARKE, M.R., DI ROCCO, T., ZERKLE, A.L., LEPLAND, A., PRAVE, A.R., MARTIN, A.P., UENO, Y., CONDON, D.J., CLAIRE, M.W. (2020) The Great Oxidation Event preceded a Paleoproterozoic “snowball Earth”. *Proceedings of the National Academy of Sciences* 117, 13314–13320. <https://doi.org/10.1073/pnas.2003901117>
- ZAHNLE, K.J., GACESA, M., CATLING, D.C. (2019) Strange messenger: A new history of hydrogen on Earth, as told by Xenon. *Geochimica et Cosmochimica Acta* 244, 56–85. <https://doi.org/10.1016/j.gca.2018.09.017>



## The end of the isotopic evolution of atmospheric xenon

L. Ardoin, M.W. Broadley, M. Almayrac, G. Avice, D.J. Byrne, A. Tarantola,  
A. Lepland, T. Saito, T. Komiya, T. Shibuya, B. Marty

### Supplementary Information

The Supplementary Information includes:

- Geological Context
- Materials and Methods
- Fluid Inclusions Study
- Fissiogenic and Mantle Contribution
- Tables S-1 to S-4
- Figures S-1 to S-4
- Supplementary Information References

### Geological Context

Hydrothermal quartz samples were selected from two different cratons based on their ages of formation, between 2.3 and 2.5 Ga, encompassing the GOE (Holland, 2006; Lyons *et al.*, 2014; Gumsley *et al.*, 2017). The Ongeluk Formation is a succession of pillowed and sheeted andesitic basalts that has undergone alteration with temperatures not exceeding 200 °C and metamorphism up to prehnite-pumpellyite facies (Cornell *et al.*, 1996; Gutzmer *et al.*, 2001, 2003). This formation is intercalated with the Makganyene glaciation deposits formed during one of the Paleoproterozoic snowball earth events (Evans *et al.*, 1997). Pods of quartz formed within the open spaces of the pillows soon after the eruption as indicated by the lack of deformation in the cavities (Gutzmer *et al.*, 2003; Saito *et al.*, 2016). The pillow-lavas are considered to have formed  $2425.6 \pm 2.6$  Ma ( $2\sigma$ ; Gumsley *et al.*, 2017) and give an upper bound to the sample. Saito *et al.*, (2018) performed Ar-Ar dating on three distinct quartz pods to estimate when the quartz crystals precipitated. They

found a maximum age of  $2701 \pm 43$  Ma ( $1\sigma$ ) and a minimum age of  $2114 \pm 312$  ( $1\sigma$ ) Ma. The difference is likely due to the difficulties in estimating the initial amount of K in the fluid. The age of  $\approx 2701$  Ma is unlikely given the age of the host rock. The petrographic description of the fluid inclusion indicates a predominantly primary origin (Saito *et al.*, 2018). Thus, the minimum age of the trapped atmospheric noble gases within the inclusions is relative to the quartz pods formed at  $2114 \pm 312$  Ma, consistent with the upper bound of the pillow lava formation.

The Seidorechka (sample FD1A) and Polisarka (sample FD3A) sedimentary formations are part of the Imandra-Varzuga Greenstone Belt. These formations were targeted by the Fennoscandian Arctic Russia – Drilling Early Earth Project (FAR-DEEP; Melezhik *et al.*, 2013) of the International Continental Scientific Drilling Program. The Imandra-Varzuga Greenstone Belt consist of several successions of alternating thin sedimentary and thick volcanic formations overlying the Archean basement (Melezhik and Sturt, 1994; Warke *et al.*, 2020). Hydrothermal quartz was collected from veins cross-cutting solely these sedimentary formations, in the shale member for FD1A and in the diamictite-greywacke member for FD3A. Depositional ages of Seidorechka and Polisarka sedimentary formations have been constrained between  $2501.5 \pm 1.7$  Ma and  $2441 \pm 1.6$  Ma (Amelin *et al.*, 1995), and  $2441 \pm 1.6$  Ma and  $2434 \pm 6.6$  Ma (Brasier *et al.*, 2013), respectively. We assumed that minerals contained in quartz veins formed contemporaneously with the overlying volcanic formations that define the minimum age of these sedimentary formations and thus yield ages of  $2441 \pm 1.6$  Ma for the quartz veins crossing Seidorechka Sedimentary Formation (FD1A ; Amelin *et al.*, 1995) and at  $2434 \pm 6.6$  Ma for the quartz veins crossing Polisarka Sedimentary Formation (FD3A ; Brasier *et al.*, 2013).

## Materials and Methods

For noble gas analyses, quartz grains of 2 to 4 mm in size were handpicked under a binocular microscope and loaded into hand-activated crushers under vacuum. Gases were extracted using a 3.5 Nm torque wrench to activate each crusher. Purified Ar and Xe gas fractions were measured using a ThermoFisher Helix MC Plus© mass spectrometer at CRPG. A total of 9 Ar and Xe analyses were performed on the Ongeluk quartz using the method of Avice *et al.* (2018) that consisted of replicated analyses on distinct crushes of 1 to 3 g of quartz. The Ar isotopic ratios were systematically analysed after each crush to check for the absence of atmospheric contamination. A new technique was used to study samples from the Kola Craton (Péron and Moreira, 2018). It consists of accumulating the extracted gases after crushing steps in an empty and previously evacuated steel bottle immersed in liquid nitrogen (77 K) during 10 minutes before purification and analysis. This method allowed the crushers to be recharged multiple times with fresh quartz grains and therefore enables the Ar and Xe gas fractions to be concentrated within the bottle. By using this method, we prepared 3 bottles for analyses: two bottles by crushing 16.70 g (FD1A-B1) and 10.08 g (FD1A-B2) of sample FD1A in 4 and 3 crusher loads respectively, and one bottle by crushing 18.16 g of sample FD3A in 4 separate crusher loads. The two



different bottles of FD1A extracted gases (FD1A – B1 and FD1A – B2) permitted the analysis of 4 and 5 aliquots of gas, respectively, to ensure reproducibility of the measurements. One bottle of extracted gases from FD3A permitted the analyses of 4 aliquots (Table S-3). The Ar abundance and isotopes were analysed only in the first gas aliquot for each bottle by multicollection. Isotopic ratios of Xe presented in Table 1 are weighted averages of the replicated analyses for each sample. For each sample, we estimated the potential mass-dependent fractionation of Xe (MDF-X, in permille per atomic mass unit  $\text{‰}\cdot\text{u}^{-1}$ , where a value of 0 indicates no MDF-Xe relative to modern atmospheric Xe) by computing linear regressions on  $^{124,126,128}\text{Xe}/^{130}\text{Xe}$  isotope ratios using the IsoplotR software (Vermeesch, 2018). Data are given with uncertainties at  $2\sigma$ .

## Fluid inclusions Study

### Petrography

Rocks of Seidorechka and Polisarka sedimentary formations are respectively crossed by 3 pluri-centimetric (5 to 10 cm) hydrothermal quartz veins. These veins are restricted to each sedimentary formation and formed after sedimentation. In these volcano-sedimentary deposits (Melezhik *et al.*, 2013), it is likely that the main fluid circulations are linked to the deposit of volcanic units overlying the sedimentary units. Thus, it is assumed that hydrothermal circulations are linked to the accumulation of Seidorechka and Polisarka volcanic formations overlying both sedimentary formations. Fluid inclusions were studied using 200- $\mu\text{m}$  doubly polished thick sections.

Sample FD1A from Seidorechka sedimentary formations does not present obvious quartz recrystallisation but shows a general pattern of parallel trails of fluid inclusions confined within individual grains. At the grain scale, inclusions are either isolated or organised within parallel trails that do not cross grain boundaries (Fig. S-1). The boundaries between grains are decorated by fluid inclusions of less than 5  $\mu\text{m}$ . The interior of the grains contains bigger inclusions, up to 20  $\mu\text{m}$ , that allowed microthermometry and Raman analyses. The inclusions are thus considered primary in origin if they are isolated or pseudo-secondary when organised in trails within the grain structure, in any case trapped during quartz growth (Roedder, 1984). All the inclusions in FD1A are biphasic with the fraction of the bubble in the range 10–20 % of the total volume. Between 5 and 10 % of the inclusions are characterised by the typical  $\text{CO}_2$  double bubble feature at room temperature (*e.g.*, Diamond, 2003).

Petrography of fluid inclusions in FD3A from Polisarka sedimentary formation is complex due to quartz deformation and recrystallisation, which resulted in (i) undulose extinction under microscope and (ii) formation of newly recrystallised grains, over ~15 % of the studied thin-section, depleted in fluid inclusions (Fig S-1; Kerrich, 1976). Given the scarcity of 1 to 5  $\mu\text{m}$  fluid inclusions within recrystallised quartz, the recrystallisation has a negligible effect on noble gas analyses compared to non-recrystallised quartz grains where most of fluid inclusions are observed. In the



latter, inclusions can be isolated, organised as trails confined within grains or as decorating quartz sub-grain boundaries. These observations are coherent with a continuous fluid entrapment contemporaneous with formation and deformation of host quartz (Eglinger *et al.*, 2014). No evidence of secondary fluid inclusions was observed. Liquid monophasic and biphasic inclusions about 10 to 20  $\mu\text{m}$  may coexist within the same grain (Fig. S-1). The volume of the vapour bubbles in biphasic inclusions varies from 80 to 20 % of the volume.

## Methods

Microthermometry was performed on fluid inclusions from samples FD1A and FD3A using a Linkam MDS600 heating-cooling stage at GeoRessources laboratory (Nancy, France). The following phase transition temperatures were measured when possible: final melting of the carbonic phase ( $T_{\text{m car}}$ ), apparent first melting of the aqueous phase ( $T_{\text{fm}}$ ), ice melting ( $T_{\text{m ice}}$ ), clathrate dissociation ( $T_{\text{m cla}}$ ), partial homogenisation of the carbon-dominated phase ( $T_{\text{h car}}$ ) and bulk homogenisation of the entire inclusion ( $T_{\text{h}}$ ). Microthermometry experiments were made between  $-150\text{ }^{\circ}\text{C}$  and not above  $200\text{ }^{\circ}\text{C}$  to avoid decrepitation. The microthermometric stage was calibrated daily using natural pure  $\text{CO}_2$  ( $-56.6\text{ }^{\circ}\text{C}$ ) and synthetic pure  $\text{H}_2\text{O}$  fluid inclusions with known transition temperatures. Precisions of the phase transition temperature measurements are about  $\pm 2\text{ }^{\circ}\text{C}$  for  $T_{\text{fm}}$ ,  $\pm 0.1\text{ }^{\circ}\text{C}$  for  $T_{\text{m car}}$ ,  $T_{\text{m ice}}$ ,  $T_{\text{fm}}$ , and  $T_{\text{m cla}}$ , and  $\pm 1\text{ }^{\circ}\text{C}$  for  $T_{\text{h}}$ .

Raman spectra were acquired at room temperature using a LabRAM HR spectrometer (Horiba Jobin Yvon) equipped with an  $1,800\text{ gr.mm}^{-1}$  grating and an edge filter at GeoRessources laboratory (Nancy, France). Excitation was provided by an  $\text{Ar}^+$  laser operating at a wavelength of  $514.53\text{ nm}$  focussed through a  $\times 50$  objective (Olympus). The aperture of the focal hole and the slit were  $500\text{ }\mu\text{m}$  and  $100\text{ }\mu\text{m}$  respectively. A total of 3 acquisitions were accumulated for each spectrum and acquisition time was variable between 60 and 10 s depending on the quality of the signal and the mobility of the bubble (shorter acquisition time for moving bubble). Spectrum acquisition was systematically performed in the quartz matrix nearby the inclusion of interest at the same depth and same analytical conditions in order to distinguish between  $\text{N}_2$  from air and  $\text{N}_2$  from the inclusion. Biphasic fluid inclusions often exhibited moving gas bubbles which prevented the acquisition of the Raman spectra. Spectra of  $\text{CH}_4$ ,  $\text{H}_2\text{S}$ ,  $\text{N}_2$  and  $\text{CO}_2$  in the gas phase were acquired separately in two different spectral windows. The absence of  $\text{H}_2$  was monitored in a third spectral window. Peak positions and areas were determined using the integration tool of LabSpec software (Horiba Jobin Yvon) at  $4156\text{ cm}^{-1}$  for  $\text{H}_2$ ;  $2917\text{ cm}^{-1}$  for  $\text{CH}_4$ ;  $2580\text{ cm}^{-1}$  for  $\text{H}_2\text{S}$  liquid;  $2331\text{ cm}^{-1}$  for  $\text{N}_2$  and the Fermi doublet at  $1285$  and  $1388\text{ cm}^{-1}$  for  $\text{CO}_2$  (Burke, 2001). The composition of biphasic inclusions in FD1A was acquired for 4 inclusions. For FD3A, 5 compositions were determined for biphasic inclusion and 8 compositions were determined for monophasic inclusions (Table S-2). The salinity of the fluid inclusions was calculated in single-salt  $\text{NaCl-CO}_2\text{-CH}_4\text{-N}_2\text{-H}_2\text{O}$  system using *Clathrates* computer package (Bakker, 1997), by using either (i) the program *ICE* following the equations of Duan *et al.*, (1996) associated with  $T_{\text{m ice}}$  and  $T_{\text{m cla}}$  when clathrate dissociation occurred in presence of ice,  $L_{\text{aq}}$  and  $\text{CO}_2$  vap,



or (ii)  $Q_2$  program when clathrate dissociation occurred via a  $Q_2$  transition (coexistence of  $L_{aq}$ , Cla,  $CO_2$  liq and  $CO_2$  vap), associated with  $T_m$  cla and  $T_h$  car and on the equations of Thiéry *et al.* (1994).

## Results

For FD1A, the observed phase transitions were  $T_{fm}$ ,  $T_m$  ice,  $T_m$  cla, and  $T_h$  for 17 inclusions (Table S-4). The  $T_{fm}$  were difficult to observe because of the small size of the fluid inclusions and the disappearance of the vapour bubble on cooling, leading to a metastable state of the inclusions until the sudden reappearance of the vapour bubble. Seven of the measured inclusions presented the typical double bubble of  $CO_2$  permitting the observation of  $T_m$  car and  $T_h$  car. The average molar composition of the vapour phase in inclusions is  $91.9 \pm 3.4$  mol %  $CO_2$ , 3.2 to 10.7 mol %  $N_2$  and  $< 1$  mol %  $CH_4$ . No significant variations were observed between biphasic and triphasic inclusion. The  $T_{fm}$  were observed from  $-21$  to  $-41$  °C and the  $T_h$  from 118 to over 200 °C. The inclusions with a  $T_{fm} \approx -21$  °C presented the lowest  $T_h$ , between 118 and 187 °C, compared to the inclusions with a lower  $T_{fm}$  which generally presented a  $T_h$  over 200 °C. These observations point to the presence of two fluids: one where the salts present in the aqueous phase are made of pure NaCl and one where they are composed of a mixing between NaCl and another salt species. The total salinity was nonetheless calculated considering pure NaCl and varies uniformly between 0.8 and 25.4 weight % in the aqueous solution independently of the salt system. It is moreover important to note that there is no apparent correlation between salinity and volatiles species concentration.

The  $T_m$  ice,  $T_m$  cla and  $T_h$  were observed for 11 biphasic inclusions in FD3A (Table S-4). Vapour and sometimes solid phases in monophasic inclusions appeared at low temperatures ( $< -120$  °C;  $n = 14$ ). Biphasic fluid inclusion vapours in sample FD3A contained  $CH_4$  from 9.8 up to 50.4 mole percent (Table S-2).  $H_2S$  was systematically present from 0.2 to 1.1 mole percent.  $N_2$  could not be distinguished from atmospheric  $N_2$  for half of the inclusions and reached a maximum of 2.4 mole percent.  $T_{fm}$  was difficult to observe in this sample and we assumed pure NaCl to calculate the salinity. It is on average  $3.3 \pm 1.9$  weight percent. The  $T_h$  were higher than 174 and generally over 200 °C. Monophasic gaseous liquid inclusions are mostly composed of  $CH_4$  (79.5 to 98.9 mole percent with one outlier at 26.2 mole percent), with minor amounts of  $H_2S$  of  $0.8 \pm 0.3$  mole percent.  $N_2$  is only present as a trace  $> 0.6$  mol %. The  $CO_2$  content varied between 4.8 and 19.5 mole percent with an outlier at 73.2 mole percent.

## Discussion and interpretation

The dominant orientation of fluid inclusions along parallel pseudo-secondary trails in FD1A sample suggests a strong tectonic influence coherent with the long-term pulsed tectonomagmatic event that affected the Imandra-Varzuga rift zone (Chashchin *et al.*, 2008). However, the tectonically influenced-fluid inclusion planes rarely cross the grains boundaries. So, these fluid inclusions are representative of the fluid, including primary noble-gas composition, present



during quartz growth. Our observations attest the preservation of two fluids within the sample. The first one characterised by pure NaCl in the aqueous phase could be assimilated to a seawater-derived fluid. The second one, where the aqueous phase contains a mixture of NaCl and another salt species, could point to a magmatic signature (Heinrich, 2005) and the analysed fluid inclusions represent a mixture between high-salinity high-temperature magmatic fluids and the low-salinity low-temperature seawater. This is in accordance with the xenon isotopic composition, which indicate a mixing between an atmospheric endmember, derived from the seawater-fluid, and a minor mantle contribution, derived from the magmatic fluid.

Sample FD3A presents heterogeneous entrapment with the coexistence of monophasic and biphasic inclusions with a continuum of size of the vapour bubbles, from 20 to 90 % of the total volume. This observation linked with the co-variation of CH<sub>4</sub>/CO<sub>2</sub> content, the monophasic liquid inclusions being enriched in the most volatiles species, are solids arguments for boiling and entrapment below the solvus within the H<sub>2</sub>O-CH<sub>4</sub>-CO<sub>2</sub>-H<sub>2</sub>S-N<sub>2</sub> system of a single fluid (Diamond, 2003). Contemporaneous recrystallisation induced the loss of some primary and pseudo-secondary fluid inclusions (Kerrick, 1976). No subsequent fluid circulation was noticed by secondary inclusions. The bulk noble gases composition issued from these fluid inclusions thus likely to reflect the composition of the late Palaeoproterozoic as this sample appears to have precipitated from one unique fluid.

## Fissiogenic and mantle contribution

### Fissiogenic contribution

Production of heavy Xe isotopes can be attributed to the spontaneous fission of <sup>238</sup>U (half-life of 4.47 Ga or <sup>244</sup>Pu (half-life of 82 Ma; Ozima and Podosek, 2002). We calculated the theoretical production of the isotopes: <sup>131</sup>Xe, <sup>132</sup>Xe, <sup>134</sup>Xe normalised to <sup>136</sup>Xe by fission of <sup>238</sup>U and <sup>244</sup>Pu (rate of production from Alexander *et al.*, 1971; Ragetti *et al.*, 1994). The Xe isotope excess was calculated as Equation S-1:

$$\left(\frac{i\text{Xe}}{^{136}\text{Xe}}\right)_{\text{excess}} = \frac{\left(\frac{i\text{Xe}}{^{130}\text{Xe}}\right)_{\text{sample}} - \left(\frac{i\text{Xe}}{^{130}\text{Xe}}\right)_{\text{atm}}}{\left(\frac{^{136}\text{Xe}}{^{130}\text{Xe}}\right)_{\text{sample}} - \left(\frac{^{136}\text{Xe}}{^{130}\text{Xe}}\right)_{\text{atm}}} \quad (\text{Eq. S-1})$$

Associated uncertainties are as Equation S-2:

$$\sigma_{\left(\frac{i\text{Xe}}{^{136}\text{Xe}}\right)_{\text{sample}}} = \left(\frac{i\text{Xe}}{^{136}\text{Xe}}\right)_{\text{sample}} \times \left[ \left( \frac{\sigma_{\left(\frac{i\text{Xe}}{^{130}\text{Xe}}\right)_{\text{sample}}}}{\left(\frac{i\text{Xe}}{^{130}\text{Xe}}\right)_{\text{sample}} - \left(\frac{i\text{Xe}}{^{130}\text{Xe}}\right)_{\text{atm}}} \right)^2 + \left( \frac{\sigma_{\left(\frac{^{136}\text{Xe}}{^{130}\text{Xe}}\right)_{\text{sample}}}}{\left(\frac{^{136}\text{Xe}}{^{130}\text{Xe}}\right)_{\text{sample}} - \left(\frac{^{136}\text{Xe}}{^{130}\text{Xe}}\right)_{\text{atm}}} \right)^2 \right]^{1/2} \quad (\text{Eq. S-2})$$

By plotting <sup>238</sup>U and <sup>244</sup>Pu fission spectrums in perspective with sample ratios, a <sup>238</sup>U origins of the heavy isotopes can be suggested for all our samples (Fig. 1; Fig. S-2)



### Mantle Contribution

The excess of  $^{129}\text{Xe}$  is thought to show a binary mixing between Archean atmosphere and mantle-derived xenon in our samples such as Equation S-3:

$$\left(\frac{^{129}}{^{130}}\right)_{\text{Sample}} = \alpha \left(\frac{^{129}}{^{130}}\right)_{\text{Mantle}} + (1 - \alpha) \times \left(\frac{^{129}}{^{130}}\right)_{\text{Archean atmosphere}} \quad (\text{Eq. S-3})$$

with  $\alpha$  as the fraction of the mantellic  $^{130}\text{Xe}$ . The value used for  $(^{129}/^{130})_{\text{Mantle}}$  is dependent on whether significant regassing of atmospheric Xe into the deep Earth is assumed to have occurred. Without regassing, we took the value  $(^{129}/^{130})_{\text{Mantle}} = 14 \pm 1$  (Marty *et al.*, 2019). Considering regassing, we assume a MORB-type composition of  $(^{129}/^{130})_{\text{Mantle}} = 6.92 \pm 0.07$  (Pető *et al.*, 2013), that is the lowest estimation in the literature (Holland and Ballentine, 2006; Mukhopadhyay, 2012; Parai and Mukhopadhyay, 2021). The calculated mantellic  $^{130}\text{Xe}$  contribution is thus an upper limit. From  $\alpha$  we calculated the associated  $(^{128}/^{130})_{\text{Expected}}$  for FD1A assuming a  $(^{128}/^{130})_{\text{Mantle}} = 0.51 \pm 0.01$  (primordial Xe, Ozima and Podosek, 2002). Results are available in Table S-1. Despite the heavy isotope discrepancies between the two bottles of FD1A, the excess of  $^{129}\text{Xe}$  is identical for the two bottles (Table S-3) so we considered an equal mantellic contribution. The difference between the excess of  $^{131}, ^{132}, ^{134}, ^{136}\text{Xe}$  is then due to a difference of crustal fissiogenic  $^{238}\text{U}$  contribution.

There is potentially a weak positive correlation among individual data in Figure S-4 with all our measurements parallel to the Rayleigh fractionation trend. This imply a similar contribution from mantle gas to the hydrothermal fluids and it does not appear realistic for samples from different locations. Within the uncertainties, the youngest sample from the Ongeluk formation is atmospheric. The excesses of  $^{129}\text{Xe}$  in the samples from the Kola Craton (Polisarka and Seidorechka formations) are consistent with the same mantle contribution to the hydrothermal fluids in this location. However, the oldest sample from Seidorechka formation presents higher  $^{128}, ^{129}\text{Xe}$  compare to the modern-air and to the Polisarka sample. This stands for a slightly fractionated atmosphere at the time that disappeared within the  $\approx 7$  million years separating the formation of the 2 samples. Without  $^{129}\text{Xe}$  excesses (this study) or deficits (Avice *et al.*, 2017; Marty *et al.*, 2019), the measurements are expected to fall on the Rayleigh fractionation trend through modern air (Fig. S-4).



## Supplementary Tables

**Table S-1** Estimation of the  $^{130}\text{Xe}$  mantellic contribution from two different endmembers composition. The Archean mantle  $^{129}\text{Xe}/^{130}\text{Xe}$  ratio is used to calculate the % mantle without crustal regassing; The MORB  $^{129}\text{Xe}/^{130}\text{Xe}$  ratio is used to calculate the % mantle with atmospheric regassing. 1 - Marty *et al.* (2019); Pepin (2003); 3 - Pető *et al.* (2013); 4 - Ozima and Podosek (2002).

|                               | $^{129}\text{Xe}/^{130}\text{Xe}$<br>( $2\sigma$ ) | $^{128}\text{Xe}/^{130}\text{Xe}$<br>( $2\sigma$ ) | Without atm regassing |   | With atm regassing    |   |
|-------------------------------|--|--|-----------------------|---|-----------------------|---|
|                               |  |  | % Mantle              | Expected<br>$^{128}\text{Xe}/^{130}\text{Xe}$ ( $2\sigma$ ) | % Mantle              | Expected<br>$^{128}\text{Xe}/^{130}\text{Xe}$ |
| FD1A                          | 6.58 (0.04)  | 0.475 (0.003)                                      | 0.9 $^{+0.3}_{-0.4}$  | 0.474 (0.001)   | 16.8 $^{+7.1}_{-5.0}$ | 0.478 $^{+0.001}_{-0.003}$                    |
| Archean Mantle <sup>1,2</sup> | 14 (1)   | 0.507 (0.004)                                      |                       |   |                       |   |
| MORB <sup>3</sup>             | 6.92 (0.07)  |  |                       |   |                       |   |
| Modern air <sup>4</sup>       | 6.50   |  |                       |   |                       |   |

**Table S-2** Molar percentage of volatiles species in some fluid inclusions determined by RAMAN spectrometry.

| N°<br>inclusion          | CO <sub>2</sub> | N <sub>2</sub> | % molar          |                 | Total   |
|--------------------------|-----------------|----------------|------------------|-----------------|---------|
|                          |                 |                | H <sub>2</sub> S | CH <sub>4</sub> |         |
| <b>FD1A - Biphasic</b>   |                 |                |                  |                 |         |
| 13                       | 88.8 %          | 10.5 %         | 0.0 %            | 0.7 %           | 100.0 % |
| 28                       | 93.4 %          | 6.5 %          | 0.0 %            | 0.1 %           | 100.0 % |
| 30                       | 95.9 %          | 3.2 %          | 0.0 %            | 0.9 %           | 100.0 % |
| 31                       | 89.3 %          | 10.7 %         | 0.0 %            | 0.0 %           | 100.0 % |
| <b>FD3A - Biphasic</b>   |                 |                |                  |                 |         |
| 1                        | 90.0 %          | 0.0 %          | 0.2 %            | 9.8 %           | 100.0 % |
| 2                        | 60.7 %          | 2.4 %          | 0.3 %            | 36.6 %          | 100.0 % |
| 3                        | 68.3 %          | 0.0 %          | 0.2 %            | 31.5 %          | 100.0 % |
| 6                        | 47.7 %          | 0.8 %          | 1.1 %            | 50.4 %          | 100.0 % |
| 9                        | 59.7 %          | 0.7 %          | 0.5 %            | 39.2 %          | 100.0 % |
| 21                       | 61.1 %          | 0.0 %          | 0.3 %            | 38.6 %          | 100.0 % |
| <b>FD3A - Monophasic</b> |                 |                |                  |                 |         |
| 1                        | 0.0 %           | 0.0 %          | 1.1 %            | 98.9 %          | 100.0 % |
| 2                        | 0.0 %           | 0.0 %          | 1.4 %            | 98.6 %          | 100.0 % |
| 3                        | 73.2 %          | 0.2 %          | 0.4 %            | 26.2 %          | 100.0 % |
| 5                        | 4.8 %           | 0.0 %          | 0.8 %            | 94.4 %          | 100.0 % |
| 8                        | 16.3 %          | 0.0 %          | 0.9 %            | 82.8 %          | 100.0 % |
| 13                       | 19.2 %          | 0.5 %          | 0.7 %            | 79.6 %          | 100.0 % |
| 14                       | 19.5 %          | 0.5 %          | 0.5 %            | 79.5 %          | 100.0 % |
| 15                       | 15.9 %          | 0.5 %          | 0.7 %            | 82.9 %          | 100.0 % |



**Table S-3** Isotopic ratio of the noble gases of each replicate. Values in red are outliers according to the Chauvenet criterion (Anscombe, 1960) and were not taken into account in the calculation of the weighted average.

**Table S-4** Observed phase transitions for FD1A biphasic fluid inclusion; FD3A biphasic and monophasic fluid inclusion and calculated NaCl weight percent associated. Value n. o. corresponds to a non-observed phase change.

Tables S-3 and S-4 can be downloaded (Excel) from the online version of the article at <https://doi.org/10.7185/geochemlet.2207>.

## Supplementary Figures

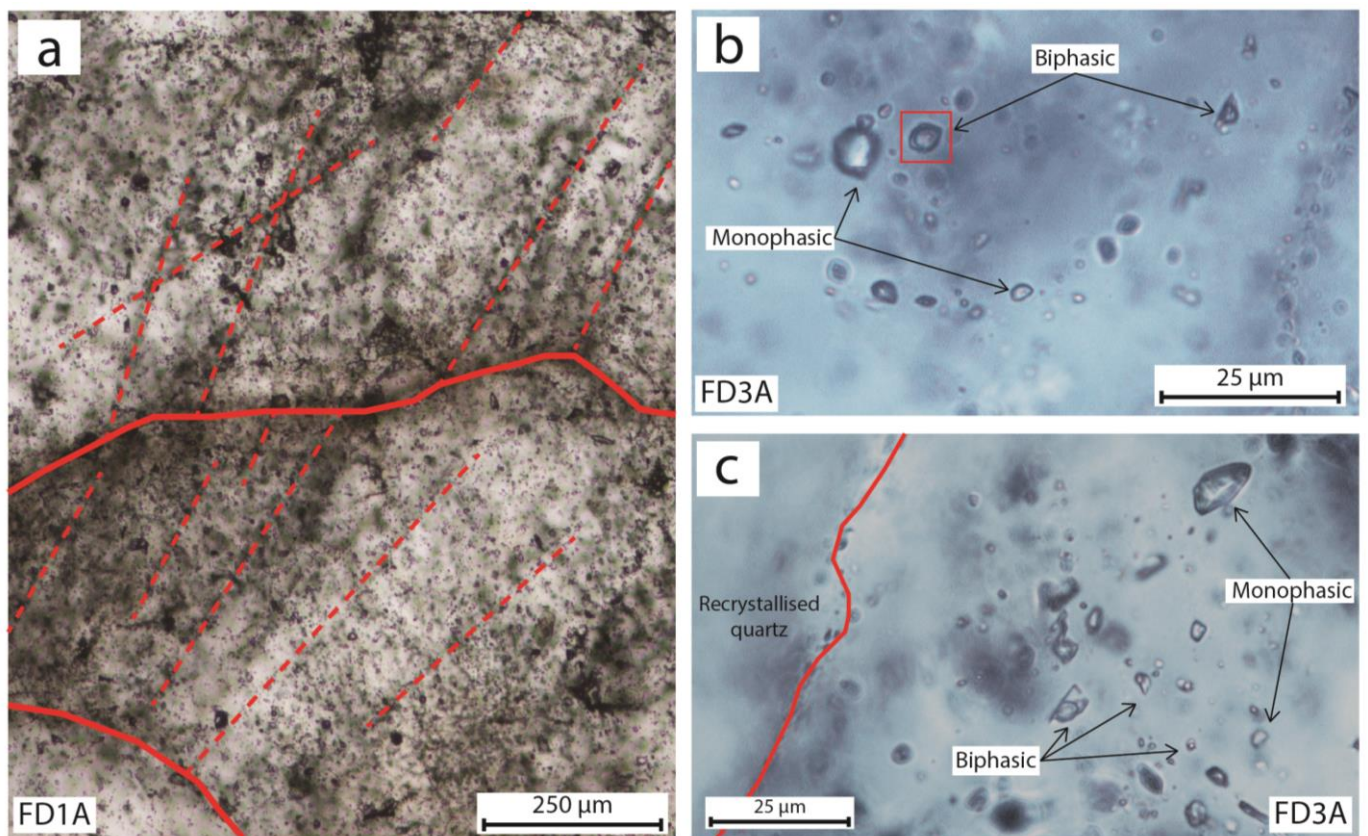


**Figure S-1** (a) Thin section photographs highlighting quartz grain boundaries (solid lines) and trails of pseudosecondary fluid inclusions (dashed lines) in FD1A. (b) Coexisting monophasic and biphasic fluid inclusions in FD3A. The red square shows a biphasic inclusion with a small rim of liquid. (c) Heterogeneous entrapment in a fluid inclusion assemblage showing the coexistence of monophasic and biphasic inclusions with variable % of vapour in FD3A characteristic of boiling process. The grain on the left is devoid of fluid inclusions as a result of recrystallisation.

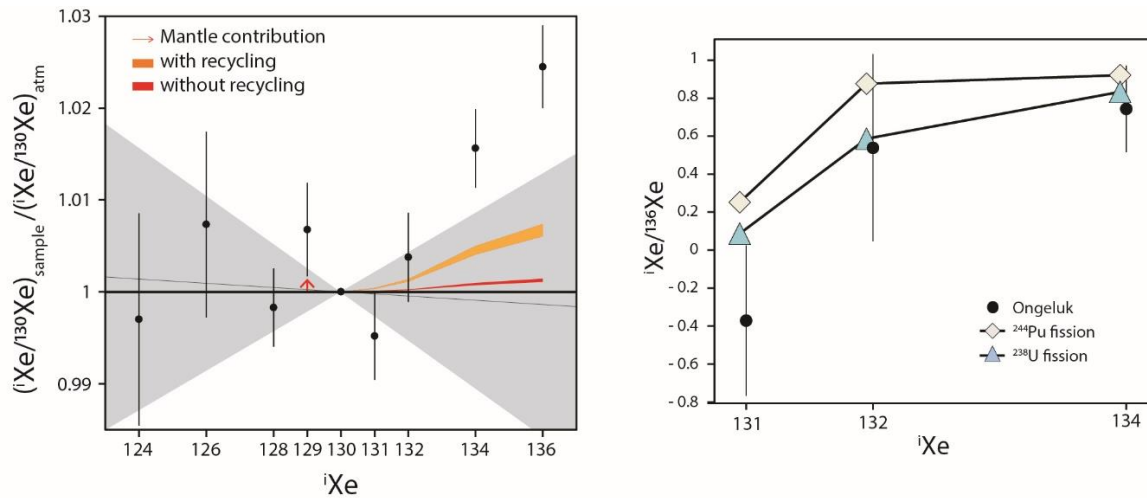


**Figure S-2** Isotopic spectra of Xe released from fluid inclusions in samples from the Ongeluk fm. Points represent the weighted average of 9 crushes of different quartz samples from the Ongeluk fm with error at  $1\sigma$ . The grey line corresponds to the isotopic trend of the  $^{124}, ^{126}, ^{128}, ^{130}\text{Xe}$  showing no mass-dependant fractionation. Error envelope is at  $2\sigma$ . The mantellic contribution is calculated considering a starting atmospheric composition as no isotopic fractionation is observed. The associated fission spectrum shows the major influence of  $^{238}\text{U}$  spontaneous fission with uncertainties at  $1\sigma$ .

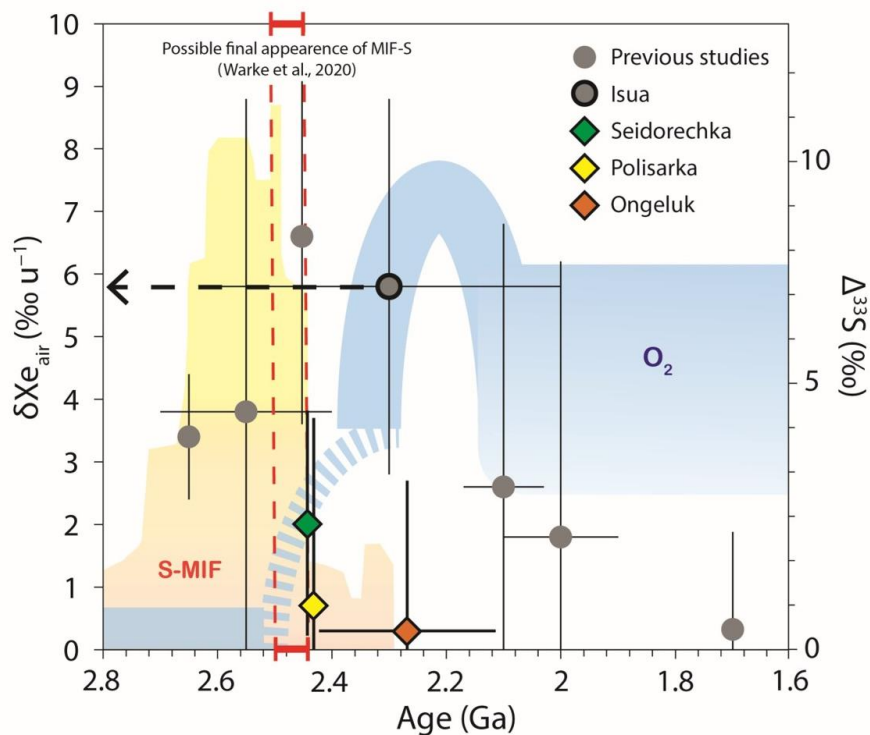


**Figure S-3** Records of atmospheric oxygen ( $\text{O}_2$ , blue; Lyons *et al.*, 2014), mass-independent fractionation of sulfur isotopes (MIF-S, orange; data from Killingsworth *et al.*, 2019) and mass dependent fractionation of xenon isotopes over the GOE period (previous data from Avice *et al.*, 2018; Almayrac *et al.*, 2021), errors are at  $2\sigma$ .



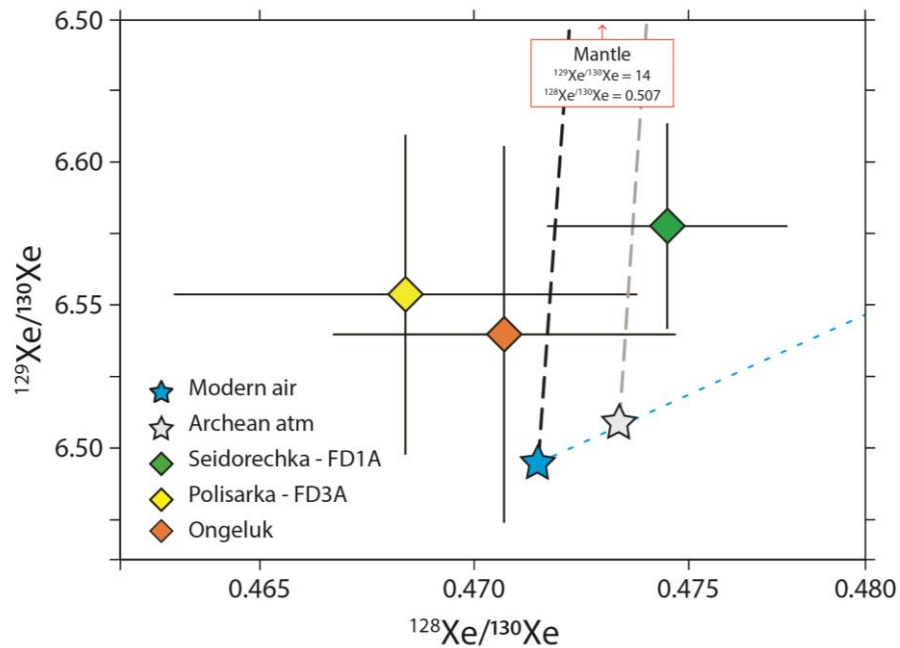


**Figure S-4** Isotopic ratios  $^{129}\text{Xe}/^{130}\text{Xe}$  vs.  $^{128}\text{Xe}/^{130}\text{Xe}$  in this study. The black (a) and grey (b) dashed lines show a mixing between a non-regassed mantle and: (a) the modern air (Ozima and Podosek, 2002); (b) the Archean atmospheric ratio calculated from FD1A. Mantle  $^{129}\text{Xe}/^{130}\text{Xe}$  composition comes from Marty *et al.* (2019) and AVCC-like  $^{128}\text{Xe}/^{130}\text{Xe}$  (Pepin, 2003). The blue dashed line shows a Rayleigh fractionation trend through modern air. Uncertainties at  $2\sigma$ .

## Supplementary Information References

- Alexander, E.C., Lewis, R.S., Reynolds, J.H., Michel, M.C. (1971) Plutonium-244: Confirmation as an Extinct Radioactivity. *Science* 172, 837-840. <https://doi.org/10.1126/science.172.3985.837>
- Almayrac, M.G., Broadley, M.W., Bekaert, D.V., Hofmann, A., Marty, B. (2021) Possible discontinuous evolution of atmospheric xenon suggested by Archean barites. *Chemical Geology* 581, 120405. <https://doi.org/10.1016/j.chemgeo.2021.120405>
- Amelin, Y.V., Heaman, L.M., Semenov, V.S. (1995) U-Pb geochronology of layered mafic intrusions in the eastern Baltic Shield : Implications for the timing and duration of Paleoproterozoic continental rifting. *Precambrian Research* 75, 31-46. [https://doi.org/10.1016/0301-9268\(95\)00015-W](https://doi.org/10.1016/0301-9268(95)00015-W)
- Anscombe, F.J. (1960) Rejection of Outliers. *Technometrics* 2, 123-146. <https://doi.org/10.1080/00401706.1960.10489888>
- Avice, G., Marty, B., Burgess, R. (2017) The origin and degassing history of the Earth's atmosphere revealed by Archean xenon. *Nature Communications* 8, 15455. <https://doi.org/10.1038/ncomms15455>
- Avice, G., Marty, B., Burgess, R., Hofmann, A., Philippot, P., Zahnle, K., Zakharov, D. (2018) Evolution of atmospheric xenon and other noble gases inferred from Archean to Paleoproterozoic rocks. *Geochimica et Cosmochimica Acta* 232, 82-100. <https://doi.org/10.1016/j.gca.2018.04.018>
- Bakker, R.J. (1997) Clathrates : Computer programs to calculate fluid inclusion V-X properties using clathrate melting temperatures. *Computers & Geosciences* 23, 1-18. [https://doi.org/10.1016/S0098-3004\(96\)00073-8](https://doi.org/10.1016/S0098-3004(96)00073-8)
- Brasier, A.T., Martin, A.P., Melezhik, V.A., Prave, A.R., Condon, D.J., Fallick, A.E. (2013) Earth's earliest global glaciation? Carbonate geochemistry and geochronology of the Polisarka Sedimentary Formation, Kola Peninsula, Russia. *Precambrian Research* 235, 278-294. <https://doi.org/10.1016/j.precamres.2013.06.007>
- Burke, E.A.J. (2001) Raman microspectrometry of fluid inclusions. *Lithos* 55, 139-158. [https://doi.org/10.1016/S0024-4937\(00\)00043-8](https://doi.org/10.1016/S0024-4937(00)00043-8)
- Chashchin, V.V., Bayanova, T.B., Levkovich, N.V. (2008) Volcanoplutonic association of the early-stage evolution of the Imandra-Varzuga rift zone, Kola Peninsula, Russia: Geological, petrogeochemical, and isotope-geochronological data. *Petrology* 16, 279-298. <https://doi.org/10.1134/S0869591108030041>



- Cornell, D.H., Schütte, S.S., Eglinton, B.L. (1996) The Ongeluk basaltic andesite formation in Griqualand West, South Africa : Submarine alteration in a 2222 Ma proterozoic sea. *Precambrian Research* 79, 101-123. [https://doi.org/10.1016/0301-9268\(95\)00090-9](https://doi.org/10.1016/0301-9268(95)00090-9)
- Diamond, L.W. (2003) Introduction to gas-bearing, aqueous fluid inclusions. *Fluid inclusions: analysis and interpretation* 32, 101-158.
- Duan, Z., Møller, N., Weare, J.H. (1996) A general equation of state for supercritical fluid mixtures and molecular dynamics simulation of mixture PVTX properties. *Geochimica et Cosmochimica Acta* 60, 1209-1216. [https://doi.org/10.1016/0016-7037\(96\)00004-X](https://doi.org/10.1016/0016-7037(96)00004-X)
- Eglinger, A., Ferraina, C., Tarantola, A., André-Mayer, A.S., Vanderhaeghe, O., Boiron, M.C., Dubessy, J., Richard, A., Brouand, M. (2014) Hypersaline fluids generated by high-grade metamorphism of evaporites : Fluid inclusion study of uranium occurrences in the Western Zambian Copperbelt. *Contributions to Mineralogy and Petrology* 167, 967. <https://doi.org/10.1007/s00410-014-0967-9>
- Gumsley, A.P., Chamberlain, K.R., Bleeker, W., Söderlund, U., de Kock, M.O., Larsson, E.R., Bekker, A. (2017) Timing and tempo of the Great Oxidation Event. *Proceedings of the National Academy of Sciences* 114, 1811-1816. <https://doi.org/10.1073/pnas.1608824114>
- Gutzmer, J., Pack, A., Lüders, V., Wilkinson, J., Beukes, N., Niekerk, H. (2001) Formation of jasper and andradite during low-temperature hydrothermal seafloor metamorphism, Ongeluk Formation, South Africa. *Contributions to Mineralogy and Petrology* 142, 27-42. <https://doi.org/10.1007/s004100100270>
- Gutzmer, J., Banks, D.A., Lüders, V., Hoefs, J., Beukes, N.J., von Bezing, K.L. (2003) Ancient sub-seafloor alteration of basaltic andesites of the Ongeluk Formation, South Africa : Implications for the chemistry of Paleoproterozoic seawater. *Chemical Geology* 201, 37-53. [https://doi.org/10.1016/S0009-2541\(03\)00225-0](https://doi.org/10.1016/S0009-2541(03)00225-0)
- Heinrich, C.A. (2005) The physical and chemical evolution of low-salinity magmatic fluids at the porphyry to epithermal transition : A thermodynamic study. *Mineralium Deposita* 39, 864-889. <https://doi.org/10.1007/s00126-004-0461-9>
- Holland, G., Ballentine, C.J. (2006) Seawater subduction controls the heavy noble gas composition of the mantle. *Nature* 441, 186-191. <https://doi.org/10.1038/nature04761>



- Holland, H.D. (2006) The oxygenation of the atmosphere and oceans. *Philosophical Transactions of the Royal Society B: Biological Sciences* 361, 903-915. <https://doi.org/10.1098/rstb.2006.1838>
- Kerrick, R. (1976) Some effects of tectonic recrystallisation on fluid inclusions in vein quartz. *Contributions to Mineralogy and Petrology* 59, 195-202. <https://doi.org/10.1007/BF00371308>
- Killingsworth, B.A., Sansjofre, P., Philippot, P., Cartigny, P., Thomazo, C., Lalonde, S.V. (2019) Constraining the rise of oxygen with oxygen isotopes. *Nature Communications* 10, 4924. <https://doi.org/10.1038/s41467-019-12883-2>
- Lyons, T.W., Reinhard, C.T., Planavsky, N.J. (2014) The rise of oxygen in Earth's early ocean and atmosphere. *Nature* 506, 307-315. <https://doi.org/10.1038/nature13068>
- Marty, B., Bekaert, D.V., Broadley, M.W., Jaupart, C. (2019) Geochemical evidence for high volatile fluxes from the mantle at the end of the Archaean. *Nature* 575, 485-488. <https://doi.org/10.1038/s41586-019-1745-7>
- Melezhik, V.A., Sturt, B.A. (1994) General geology and evolutionary history of the early proterozoic Polmak-Pasvik-Pechenga-Imandra/Varzuga-Ust'Ponoy greenstone belt in the northeastern Baltic Shield. *Earth-Science Reviews* 36, 205-241. [https://doi.org/10.1016/0012-8252\(94\)90058-2](https://doi.org/10.1016/0012-8252(94)90058-2)
- Melezhik, V.A., Prave, A.R., Lepland, A., Hanski, E.J., Romashkin, A.E., Rychanchik, D.V., Luo, Z.Y., Sharkov, E.V., Bogina, M.M., Brasier, A.T., Fallick, A.E. (2013) 6.1 The Imandra/Varzuga Greenstone Belt. In: Melezhik, V., Prave, A.R., Hanski, E.J., Fallick, A.E., Lepland, A., Kump, L.R., Strauss, H. (Eds.) *Reading the Archive of Earth's Oxygenation*. Springer Berlin Heidelberg, 505-590. [https://doi.org/10.1007/978-3-642-29659-8\\_2](https://doi.org/10.1007/978-3-642-29659-8_2)
- Mukhopadhyay, S. (2012) Early differentiation and volatile accretion recorded in deep-mantle neon and xenon. *Nature* 486, 101-104. <https://doi.org/10.1038/nature11141>
- Ozima, M., Podosek, F.A. (2002) *Noble Gas Geochemistry*. Second Edition, Cambridge University Press, Cambridge. <https://doi.org/10.1017/CBO9780511545986>
- Parai, R., Mukhopadhyay, S. (2021) Heavy noble gas signatures of the North Atlantic Popping Rock 2IID43 : Implications for mantle noble gas heterogeneity. *Geochimica et Cosmochimica Acta* 294, 89-105. <https://doi.org/10.1016/j.gca.2020.11.011>
- Pepin, R.O. (2003) On Noble Gas Processing in the Solar Accretion Disk. In: Kallenbach, R., Encrenaz, T., Geiss, J., Mauersberger, K., Owen, T.C., Robert, F. (Eds.) *Solar System History from Isotopic Signatures of Volatile Elements:*



*Volume Resulting from an ISSI Workshop 14–18 January 2002*, Springer Netherlands, Bern, 211–230.

[https://doi.org/10.1007/978-94-010-0145-8\\_14](https://doi.org/10.1007/978-94-010-0145-8_14)

Péron, S., Moreira, M. (2018) Onset of volatile recycling into the mantle determined by xenon anomalies. *Geochemical Perspectives Letters* 9, 21–25. <https://doi.org/10.7185/geochemlet.1833>

Pető, M.K., Mukhopadhyay, S., Kelley, K.A. (2013) Heterogeneities from the first 100 million years recorded in deep mantle noble gases from the Northern Lau Back-arc Basin. *Earth and Planetary Science Letters* 369–370, 13–23.

<https://doi.org/10.1016/j.epsl.2013.02.012>

Ragettli, R.A., Hebeda, E.H., Signer, P., Wieler, R. (1994) Uranium-xenon chronology: Precise determination of  $\lambda_{sf} * 136Y_{sf}$  for spontaneous fission of  $^{238}U$ . *Earth and Planetary Science Letters* 128, 653–670. [https://doi.org/10.1016/0012-](https://doi.org/10.1016/0012-821X(94)90177-5)

[821X\(94\)90177-5](https://doi.org/10.1016/0012-821X(94)90177-5)

Roedder, E. (1984) *Fluid inclusions*. Reviews in Mineralogy, Vol. 12. Mineralogical Society of America, Virginia.

Saito, T., Shibuya, T., Komiya, T., Kitajima, K., Yamamoto, S., Nishizawa, M., Ueno, Y., Kurosawa, M., Maruyama, S. (2016)

PIXE and microthermometric analyses of fluid inclusions in hydrothermal quartz from the 2.2Ga Ongeluk Formation, South Africa : Implications for ancient seawater salinity. *Precambrian Research* 286, 337–351.

<https://doi.org/10.1016/j.precamres.2016.10.003>

Saito, T., Qiu, H.N., Shibuya, T., Li, Y.B., Kitajima, K., Yamamoto, S., Ueda, H., Komiya, T., Maruyama, S. (2018) Ar–Ar dating for hydrothermal quartz from the 2.4 Ga Ongeluk Formation, South Africa : Implications for seafloor hydrothermal

circulation. *Royal Society Open Science* 5, 180260. <https://doi.org/10.1098/rsos.180260>

Thiéry, R., Kerkhof, A., Dubessy, J. (1994) vX properties of CH<sub>4</sub>-CO<sub>2</sub> and CO<sub>2</sub>-N<sub>2</sub> fluid inclusions : Modelling for T < 31°C and

P < 400 bars. *European Journal of Mineralogy* 6, 753–771. <https://doi.org/10.1127/ejm/6/6/0753>

Vermeesch, P. (2018) IsoplotR : A free and open toolbox for geochronology. *Geoscience Frontiers* 9, 1479–1493.

<https://doi.org/10.1016/j.gsf.2018.04.001>

Warke, M.R., Di Rocco, T., Zerkle, A.L., Lepland, A., Prave, A.R., Martin, A.P., Ueno, Y., Condon, D.J., Claire, M.W. (2020)

The Great Oxidation Event preceded a Paleoproterozoic “snowball Earth”. *Proceedings of the National Academy of Sciences* 117, 13314–13320. <https://doi.org/10.1073/pnas.2003090117>

